

1 **Revision2**

2 **High-temperature structural change and microtexture formation of sillimanite and its**  
3 **phase relation with mullite**

4 **Yohei Igami<sup>1,2\*</sup>, Shugo Ohi<sup>3</sup>, Tetsu Kogiso<sup>4</sup>, Noboru Furukawa<sup>5</sup>, and Akira Miyake<sup>1</sup>**

5 <sup>1</sup> Graduate School of Science, Kyoto University, Kyoto 606-8502, Japan

6 <sup>2</sup> Institute of Materials and Systems for Sustainability, Nagoya University, Nagoya  
7 464-8603, Japan

8 <sup>3</sup> Faculty of Education, Shiga University, Ohtsu 520-0862, Japan

9 <sup>4</sup> Graduate School of Human and Environmental Studies, Kyoto University, Kyoto  
10 606-8501, Japan

11 <sup>5</sup> Graduate School of Science, Chiba University, Chiba 263-8522, Japan

12 \*Corresponding author. E-mail: [y-igami@nagoya-u.jp](mailto:y-igami@nagoya-u.jp)

13

14

### **Abstract**

15 Synchrotron powder X-ray diffraction (XRD) experiments and transmission electron  
16 microscopy (TEM) observations of heat-treated sillimanite at various pressures were  
17 conducted to clarify the detailed phase relation between sillimanite and mullite. Under  
18 TEM, heat-treated sillimanite frequently showed anti-phase boundary (APB)-like textures

19 with a displacement vector of  $1/2[001]_{\text{sil}}$ . Additional scanning TEM-energy dispersive  
20 X-ray spectroscopy analysis of regions with APB-like texture showed that they were clearly  
21 enriched in Al and accompanied by very fine, Si-rich glass inclusions, which indicates that  
22 the APB-like textures are composed of fine mullite. Moreover, synchrotron XRD patterns  
23 of these samples clearly showed double peaks of newly formed mullite and remnant  
24 sillimanite, indicating that the compositional transformation from sillimanite to mullite and  
25 glass is discontinuous. We separately determined the cell parameters of the sillimanite and  
26 mullite from the XRD pattern and found that the  $b$  axial length of the sillimanite increased  
27 with the treatment temperature, reflecting disordering of tetrahedral Al and Si in the  
28 sillimanite. In contrast, the positions of the deconvoluted mullite peaks indicated that the  $a$   
29 axial length of mullite decreased as experimental pressure increased, owing to enrichment  
30 of the Si component. By projecting the cell parameters onto the  $a$ - $b$  axial plane, the  
31 detailed changes in the crystallographic state of the sillimanite and mullite could be easily  
32 and comprehensively identified. On the basis of our results, we propose a new  $P$ - $T$  diagram  
33 for the  $\text{Al}_2\text{SiO}_5$  system that shows the transformation boundary between sillimanite and  
34 mullite +  $\text{SiO}_2$ -rich melt and the contour of the Al/Si order parameter of sillimanite.

35 **Keywords:** sillimanite, mullite, high-temperature phase relation, TEM observation,  
36 synchrotron X-ray experiment

37

## Introduction

38

39 Naturally occurring polymorphs of  $\text{Al}_2\text{SiO}_5$  (andalusite, kyanite, sillimanite) have  
40 assumed a special significance for geologists because of their abundance in metamorphic  
41 rocks and their simple pressure–temperature ( $P$ – $T$ ) phase relations. Although the phase  
42 relations in this system have been investigated over many years, however, some problems  
43 persist, in particular, related to sillimanite.

44 The crystal structure of sillimanite [space group  $Pbnm$  (No. 62)] is characterized by  
45 chains of edge-sharing  $\text{AlO}_6$  octahedra ( $\text{AlO}_4$  octahedral chains) linked to double  
46  $\text{SiO}_4/\text{AlO}_4$  tetrahedral chains parallel to the  $c$ -axis, with the  $\text{SiO}_4$  and  $\text{AlO}_4$  tetrahedra  
47 arranged alternately. Zen (1969) considered that disordering of this tetrahedral Al and Si  
48 arrangement in sillimanite might be an important factor leading to complications of the  
49  $\text{Al}_2\text{SiO}_5$  phase equilibria. Subsequently, other researchers (e.g., Holdaway 1971;  
50 Greenwood 1972; Saxena 1974) have also suggested that Al/Si disordering in sillimanite,  
51 which increases the configuration entropy, might have important effects on the phase  
52 relations of  $\text{Al}_2\text{SiO}_5$  polymorphs.

53 Navrotsky et al. (1973) experimentally detected an enthalpy difference between  
54 untreated sillimanite and sillimanite heated at 1200–1700 °C under pressures of 1.6–2.3  
55 GPa that they inferred to reflect Al/Si disordering. However, Holland and Carpenter (1986),  
56 using transmission electron microscopy (TEM), observed small glass inclusions in  
57 sillimanite samples heat-treated under conditions similar to those used by Navrotsky et al.  
58 (1973). They inferred that some transformation related to mullite [ $\text{Al}_2(\text{Al}_{2+2x}\text{Si}_{2-2x})\text{O}_{10-x}$ ,  
59 where  $x = 0.17$ – $0.59$  (Cameron 1977), space group  $Pbam$  (No. 55)], which is more Al-rich

60 than sillimanite, had occurred as a result of partial melting at high temperatures, and that  
61 the enthalpy change detected by Navrotsky et al. (1973) might in part reflect the appearance  
62 of similar fine glass inclusions. These results imply that experimental investigation of the  
63 degree of Al/Si order in sillimanite at high temperatures is not simple; rather, careful  
64 differentiation between sillimanite and mullite, including glass phases, is very important.

65         However, sillimanite and mullite are difficult to distinguish because of the similarity  
66 of their crystal structures. Mullite has the same basic framework as sillimanite (i.e.,  $\text{AlO}_4$   
67 octahedral chains and double  $\text{SiO}_4/\text{AlO}_4$  tetrahedral chains), and its structure differs from  
68 that of sillimanite only by the disordered distribution of Al and Si in the tetrahedra and the  
69 existence of an additional tetrahedral site, which is coupled to the occurrence of oxygen  
70 vacancies (e.g., Fischer et al., 2012). In fact, Burnham (1963) reported that only a few  
71 atoms need to be slightly shifted or removed to create one phase from the other.

72         Moreover, the exact phase relation and the  $P$ – $T$  boundary between the two phases is  
73 still not clear. Some researchers (e.g., Hariya et al. 1969) have suggested that there may be  
74 a complete solid solution series between sillimanite and mullite under certain high  
75 temperature and high pressure conditions, although it is relatively accepted that a  
76 miscibility gap exists at around  $0.04 < x \leq 0.17$  in  $\text{Al}_2(\text{Al}_{2+2x}\text{Si}_{2-2x})\text{O}_{10-x}$  (Cameron 1977). In  
77 addition, Fischer et al. (2015) newly reported a natural mineral, “sillimullite” that is  
78 intermediate between sillimanite and mullite but different to both of them.

79         Furthermore, there are large inconsistencies among previous estimates of the phase  
80 boundary position on the  $P$ – $T$  diagram (e.g., Holm and Kleppa 1966; Weill 1966; Kiseleva  
81 et al. 1983). The ambiguities regarding the phase relation between sillimanite and mullite

82 have prevented precise phase identifications and inhibited further investigations of Al/Si  
83 disordering in sillimanite.

84 Recently, Igami et al. (2017), using a synchrotron X-ray and high-resolution  
85 multiple-detector system developed by Toraya et al. (1996), successfully distinguished the  
86 X-ray diffraction (XRD) peaks of sillimanite and mullite in mixtures of these two minerals.  
87 In this study, therefore, we conducted experiments in which we treated sillimanite samples  
88 under various  $P$ - $T$  conditions, and then we used the synchrotron XRD system and  
89 TEM-energy dispersive spectroscopy (EDS) to analyze the results. In particular, we  
90 re-examined the phase relation between sillimanite and mullite with consideration of the  
91 degree of Al/Si order in sillimanite by applying these methods to the investigation of  
92 submicroscopic textures and precise cell-parameter relations. On the basis of our results, we  
93 propose a new  $P$ - $T$  diagram of the high-temperature region in the  $\text{Al}_2\text{SiO}_5$  system.

94

95

96

## Sample preparation

### Starting material

98 As starting material (hereafter, STR), we used sillimanite crystals from the same  
99 sample (collected in Rundvågshetta, East Antarctica; RVH92011102A, Kawasaki et al.  
100 1993, 2011) that we used in our previous experiments (Igami et al. 2017, 2018a). The XRD  
101 pattern of STR shows only sillimanite peaks, and its cell parameters are  $a = 7.4867(6)$ ,  $b =$   
102  $7.6750(5)$ , and  $c = 5.7720(5)$  Å (Igami et al., 2018). Its chemical composition, determined  
103 by scanning electron microscopy (SEM)-EDS, is  $\text{Al}_{1.99}\text{Fe}_{0.01}\text{Si}_{1.00}\text{O}_5$  (Igami et al. 2017).

104 Under TEM, STR has no characteristic textures such as anti-phase boundary (APB)  
105 textures, lamellae, or inclusions (Igami et al. 2018a). The STR crystals were crushed, and  
106 impurities were removed under an optical microscope. Then, crystals of adequate size (~2  
107 mm across) were picked out for use as single-crystal samples. The rest of the sample was  
108 ground to powder, and then powdered samples were loaded into 3-mm-diameter platinum  
109 capsules and then both sides of the capsule were squeezed flat for the heating experiment.

110

### 111 **Heat treatments**

112 Both the single-crystal and powdered samples were subjected to various  
113 temperatures and pressures. A muffle furnace was used for experiments at ambient pressure  
114 (1 atm), and an internally heated pressure vessel or piston-cylinder apparatus was used for  
115 experiments at high pressure (HP). Hereafter, experimental samples treated at temperature  
116  $T$ , pressure  $P$ , for time  $t$  are designated as S\_ $T$ - $P$ - $t$  (e.g., S\_790°C-1atm-700h)

117

118 **Muffle furnace.** Both single-crystal and powdered samples were placed in a platinum  
119 crucible and heated in a muffle furnace (Nabertherm, LHT02/17 or Koyo, KBF314N1) at 1  
120 atm and temperatures of 790 to 1530 °C for 1 to 1711 h. The temperature was measured  
121 with a Pt<sub>70</sub>Rh<sub>30</sub>-Pt<sub>94</sub>Rh<sub>6</sub> (B-type) thermocouple placed at the top of the sample space in the  
122 furnace. A digital program controller maintained the run temperature within ±1 °C of the  
123 nominal value. After heating, the samples were allowed to cool at a cooling rate of ~10  
124 °C/min. Igami et al. (2018a) previously observed some of these samples by TEM and used  
125 high angular resolution electron channeling X-ray spectroscopy (HARECXs) to determine

126 their Al/Si order parameters.

127

128 **Internally heated pressure vessel.** HP experiments at the pressure of 0.2 GPa were  
129 performed in an internally heated pressure vessel (KOBELCO, Dr. HIP) at Chiba  
130 University. A powdered sample in a Pt capsule or a single-crystal sample was placed in a  
131 platinum wire cage in the internally heated pressure vessel and subjected to temperatures  
132 from 1200 to 1400 °C. The pressurizing medium was Ar gas, and the pressure was  
133 maintained within  $\pm 0.002$  GPa of the nominal pressure of 0.2 GPa during all experiments.  
134 The run temperature was monitored with a Pt–Pt<sub>87</sub>Rh<sub>13</sub> (R-type) thermocouple in the vessel  
135 and maintained within  $\pm 1$  °C of the nominal value. After the heat treatment, samples were  
136 allowed to cool at a cooling rate of  $\sim 100$  °C /min.

137

138 **Piston-cylinder apparatus.** HP experiments at pressures of 0.5–2.5 GPa were performed  
139 in a Boyd-England type piston-cylinder apparatus with a 1/2-inch-diameter cylinder and  
140 piston (C&T Factory, PG-100) at Kyoto University. Powdered samples in Pt capsules were  
141 placed in a MgO holder that was surrounded by graphite heaters, Pyrex glass and talc  
142 sleeves, and subjected to temperatures from 1300 to 1500 °C. In these experiments,  
143 single-crystal samples were not used. The pressure was maintained within  $\pm 0.2$  GPa of the  
144 nominal pressure during all experiments. The pressure calibration was previously carried  
145 out using silica and enstatite phase transformations (Machida et al. 2017). The run  
146 temperature was monitored with a Pt–Pt<sub>87</sub>Rh<sub>13</sub> (R-type) thermocouple and a digital program  
147 controller (CHINO, KP100c) maintained the temperature within  $\pm 1$  °C of the nominal value.

148 The thermal gradient of the assembly was previously shown to be limited by an  
149 investigation of the run charge of an enstatite–diopside mixture (Machida et al. 2017). After  
150 the heat treatment, samples were allowed to cool at a cooling rate of ~100 °C/sec.

151

152

## **Experimental methods**

### **153 Synchrotron powder XRD experiments**

154 The powdered samples were analyzed by XRD using the multiple-detector system  
155 of Toraya et al. (1996) and the BL-4B<sub>2</sub> beamline at the Photon Factory of the High Energy  
156 Accelerator Research Organization, Tsukuba, Japan. The segmented intensity data were  
157 connected after adjustment for peak shifts and detector sensitivities (Ida 2005). The step  
158 interval for scanning was 0.005 or 0.010°, and the diffraction angles ranged from 8.000 to  
159 150.000° 2 $\theta$ . Because this XRD system is shared by several users, the measurements were  
160 performed over several intervals. Before each measurement interval, we therefore measured  
161 the Si powder standard (NIST SRM640c) and STR. The peak wavelength of the source  
162 X-ray beam was determined by analysis of the diffraction peak profiles of the Si powder  
163 (Ida et al. 2003). The wavelengths of the X-ray beam were determined to be 1.747061(11),  
164 1.746881(11), 1.746985(10), 1.197419(7), and 1.197318(21) Å. Zero shift and eccentric  
165 error for each measurement interval were optimized by analysis of the diffraction peaks of  
166 STR.

167

### **168 TEM and scanning TEM observations**

169 A focused ion beam (FIB) system (Thermo Fisher Scientific Quanta 200 3DS or



170 Helios NanoLab G3 CX) was used to prepare ultrathin sections of 16 single-crystal samples  
171 for TEM observations. The sections of crystal samples from the muffle furnace and  
172 internally heated pressure vessel treatments and the powdered samples from the  
173 piston-cylinder treatment were embedded in epoxy resin and then polished to a smooth  
174 surface. Using the FIB system, a predefined area (20–30  $\mu\text{m}^2$ ) was coated with Pt and then  
175 a  $\text{Ga}^+$  ion gun was used to cut out the surrounding material to a depth of  $\sim 10 \mu\text{m}$ . Then the  
176 section was cut off, mounted on a TEM grid, and thinned to a thickness of  $\sim 150 \text{ nm}$  using a  
177  $\text{Ga}^+$  ion beam at 30 kV with beam currents of 0.1–3 nA. In the final processing, a  $\text{Ga}^+$  ion  
178 beam at 5 kV with a beam current of 48 pA was used to remove amorphous layers from the  
179 surface of the sections.

180 The samples were studied under a JEOL JEM-2100F transmission electron  
181 microscope operated at 200 kV at Kyoto University. TEM images were recorded by CCD  
182 cameras (Gatan, Orius 200D and 1000D). Selected area electron diffraction (SAED)  
183 patterns of mullite and sillimanite are similar, but show one important difference. In the  
184 case that a SAED pattern is indexed based on the standard cell of sillimanite,  $l = \text{odd}$   
185 reflections are typical for sillimanite, but they are absent for mullite, as also described by  
186 Igami et al. (2018a). Samples were observed by dark field (DF) imaging taken from  $l = \text{odd}$   
187 reflections of sillimanite as well as by bright field (BF) imaging.

188 Because mullite is slightly enriched in  $\text{Al}_2\text{O}_3$  compared with sillimanite, chemical  
189 analyses were performed by annular dark-field scanning TEM (ADF-STEM) with X-ray  
190 mapping using a TEM equipped with annular STEM and EDS detectors (JEOL JED2300T).  
191 The acceptable angle of the STEM detector was set to approximately 50–150 mrad to

192 reflect the atomic numbers of the constituent elements (high-angle annular dark-field  
193 STEM image). Moreover, a simple k-factor method was used to evaluate the Al/Si ratio of  
194 some samples. The *k*-factor of Al-K to Si-K ( $k_{\text{Al/Si}}$ ) was calibrated by using the STEM-EDS  
195 results for STR. By the STEM-EDS analysis of 12 different regions of STR, the  $I_{\text{(Al-K)}}/I_{\text{(Si-K)}}$   
196 X-ray count ratio converged to an average value of 2.09 with a standard error of 0.02. From  
197 this result, the *k*-factor was determined to be  $k_{\text{Al/Si}} = 0.96$ , to adjust the Al/Si compositional  
198 ratio of STR to 2.00. This *k*-factor includes the effect of X-ray absorption, but errors caused  
199 by the X-ray absorption effect were assumed to be small, because FIB was used to make  
200 the thickness of all of the TEM sections almost the same and because the absorption  
201 coefficients of Al-K and Si-K are similar.

202

203

204

## Results and Discussion

### 205 **Phase identification in high-resolution XRD patterns**

206 The high-resolution XRD patterns of some heat-treated samples are similar to that  
207 of STR, but exhibited small new peaks and a broad glass halo, same as Igami et al. (2017).  
208 Peak positions of this newly appeared phase and sillimanite are so close to each other that  
209 they cannot be separated from their mixtures in laboratory XRD systems. Our XRD  
210 patterns indicate that the newly appeared phases show no diffraction peaks at the positions  
211 corresponding to the reflections with  $l = \text{odd}$  in the case of indexing based on the unit cell  
212 of sillimanite (Fig. 1, showing the case of S\_1476°C-1atm-10h). This indicates that the  
213 appeared phase is changed in translational symmetry with half the size of the  $c$  axial length  
214 from sillimanite. It is most likely that mullite was formed from sillimanite with partial  
215 melting, although there remains a little possibility that the  $l = \text{odd}$  reflections are so weak  
216 that they cannot be detected in the multiphase patterns and the new phase might be a special  
217 mullite with doubled  $c$  parameter similar to the "sillimullite" described by Fischer et al.  
218 (2015). Some XRD patterns of HP-treated samples also included corundum peaks. The only  
219 detected phases in the XRD patterns were sillimanite, mullite, corundum, and glass. All  
220 detected crystalline phases in the samples are listed in Tables 1, 2. Clear mullite peaks were  
221 detected only in samples heated above 1200 °C.

222

### 223 **Peak shifts of sillimanite and mullite detected in high-resolution XRD patterns**

224 Compared with STR, the XRD patterns of heat-treated sillimanite at 1 atm seemed  
225 to show a slight peak shift as the treatment temperature increased (Fig. 2a). These peak

226 shifts, which were detected even though all of the XRD experiments were performed at  
227 room temperature, indicate slight changes in the crystal structure of the sillimanite except  
228 for thermal expansion or transformation to mullite. In samples treated by both heating and  
229 pressure, the XRD patterns also showed a shift in the mullite peak position (Fig. 2b). Thus,  
230 mullite seemed to change its crystallographic state as treatment temperature and pressure  
231 increased, and the pressure effect was likely more effective than the temperature effect as a  
232 cause of the structural change.

233 We evaluated these peak position differences by calculating the cell parameters of  
234 all of the experimental samples from the XRD patterns by least-squares fitting. Before the  
235 calculation, we carefully deconvoluted the peaks of sillimanite and mullite using the  
236 pseudo-Voigt function, taking advantage of the high angular resolution of the XRD system.  
237 The determined cell parameters are listed in Tables 1–2, and details are discussed later.

238

### 239 **TEM observations of microtextures**

240 Under TEM, the experimental samples showed various microtextures that were  
241 different from those of STR (Table 3). For example, TEM images and SAED patterns of  
242 S\_1476°C-1atm-696h, the XRD pattern of which showed only mullite + glass, are shown in  
243 Figure 3. When SAED patterns are indexed according to the standard cell of sillimanite,  
244 reflections with  $l = \text{odd}$  (e.g., 021) are extinct, which indicates mullite. In this sample, many  
245 characteristic glass inclusions elongated in the direction of the  $c$ -axis of the host mullite  
246 were observed (Fig. 3a) with characteristic shapes bounded by the  $\{110\}$  prismatic planes  
247 of mullite (Fig. 3b). This texture is similar to that reported by previous TEM studies (e.g.,

248 Holland and Carpenter 1986; Raterron et al. 1999, 2000), and these inclusions should  
249 correspond to the glass halo in the XRD patterns. STEM-EDS analysis using  $k_{\text{Al/Si}} = 0.96$  of  
250 five different mullite regions without inclusions yielded an average Al/Si ratio = 3.02(10),  
251 which is consistent with the normal (3:2) mullite composition:  $3\text{Al}_2\text{O}_3 \cdot 2\text{SiO}_2$  (Al/Si = 3.00).

252 Figure 4 shows TEM images and SAED patterns of S\_1450°C-1atm-1150h, which  
253 was ~77% transformed to mullite + glass with ~23% remaining as sillimanite, as  
254 determined by Igami et al. (2017). Two regions are seen in the DF image taken from the  $l =$   
255 odd reflection of sillimanite (Fig. 4a): a dark appearing mullite region and a bright  
256 appearing sillimanite region. The mullite region has the same characteristics as  
257 S\_1476°C-1atm-696h (Fig. 3), whereas the residual sillimanite region exhibits textures like  
258 anti-phase boundaries (APB-like texture) with a displacement vector of  $1/2[001]$ . Glass  
259 inclusions were observed along with these textures, although they were very fine. Holland  
260 and Carpenter (1986) described similar APB-like textures in their TEM study.

261 APB-like textures visualized by DF-TEM imaging of  $l =$  odd reflections were also  
262 observed in many samples that did not clearly show mullite regions. For example, Figure 5  
263 shows an APB-like texture in S\_1373°C-1atm-300h, ~24% of which was transformed to  
264 mullite + glass with ~76% remaining as sillimanite, as determined by Igami et al. (2017). In  
265 this TEM section, no clear mullite regions are present, but APB-like textures are observed  
266 (Fig. 5b). The ADF-STEM image and X-ray map (Figs. 5d, e) clearly show that the regions  
267 with these textures are more Al rich than the host sillimanite, and they are accompanied by  
268 fine Si-rich inclusions. This observation indicates that the regions with APB-like texture are  
269 not compositionally the same as the host but consist of mullite accompanied by fine

270 SiO<sub>2</sub>-rich glass inclusions. These APB-like mullite textures were not observed in samples  
271 heated to less than 1140 °C; this result is consistent with our XRD results and with the  
272 mullitization temperature determined by Igami et al. (2017).

273 Figure 6 shows the TEM images of S\_1400°C-1GPa-52h, which is composed of  
274 both sillimanite and mullite grains, identified by their SAED patterns. The mullite grains  
275 have fewer glass inclusions than those in samples heat-treated at 1 atm. STEM-EDS  
276 analysis of 10 different mullite regions yielded an average Al/Si ratio of 2.43(6), calculated  
277 using  $k_{\text{Al/Si}} = 0.96$ . This composition is intermediate between sillimanite (Al/Si = 2.00) and  
278 3:2 mullite (Al/Si = 3.00), but it is within the mullite solid solution series proposed by  
279 Cameron (1977). Based on both the SAED and EDS results, this phase is referred to as  
280 siliceous mullite. The DF image of the  $l = \text{odd}$  reflection in a sillimanite grain showed  
281 APB-like textures but fewer glass inclusions than the samples heat treated at 1 atm. This  
282 result indicates that the regions with APB-like textures are also composed of siliceous  
283 mullite with relatively few glass inclusions. These findings support the inference of Hariya  
284 et al. (1969), deduced by XRD analysis, that siliceous mullite is formed at high pressures.

285

### 286 **Cell parameter variation against treatment temperature**

287 Figure 7 shows the determined cell parameters (Tabs. 1, 2) against treatment  
288 temperature. In the figure, the  $b$  axial length showed the most marked expansion, although  
289 the cell parameter that differs most between sillimanite and mullite is the  $a$  axial length.  
290 Igami et al. (2018a) determined that the Al/Si order parameter  $Q$  of the tetrahedral site in  
291 sillimanite, excluding mullite and glasses in the same sample. The  $Q$  value varies from 1

292 for total order to 0 to total disorder, and is given as  $Q = 2p - 1$  in the case of stoichiometric  
293 sillimanite, where  $p$  is the probability of finding an Al (Si) atom on a Al (Si) site. The  
294 results of Igami et al. (2018a) shows that  $Q$  decreases continuously as the treatment  
295 temperature increases. Therefore, this characteristic change in the  $b$  axial length can be  
296 attributed to Al/Si disordering in sillimanite. We plotted the  $Q$  values determined by Igami  
297 et al. (2018a) against  $b$  axial length (Fig. 8) and found that the relation between  $Q$  and  $b$   
298 tends to be negative and approximately linear, at least for  $Q > 0.7$ . According to Igami et al.  
299 (2018a), this range of  $Q$  corresponds to heating temperatures  $T < \sim 1400$  °C. It is not clear  
300 whether the relation is linear for  $Q < 0.7$ , corresponding to  $T > \sim 1400$  °C, but temperatures  
301 in this range are too high to be applicable to natural metamorphic processes. This result  
302 indicates that under metamorphic geological conditions, the order parameter  $Q$  of  
303 sillimanite can be roughly estimated from the  $b$  axial length of the sillimanite.

304 Sillimanite in HP-treated samples changes with increasing treatment temperature  
305 similarly to sillimanite in samples heated at 1 atm (Fig. 7, right panels). This result  
306 indicates that the pressure condition does not significantly affect Al/Si disordering and is in  
307 agreement with the assumption of Greenwood (1972). Two mullite samples (arrows in Fig.  
308 7a, left panel) with  $a = \sim 7.52$  Å plot between the sillimanite and mullite groups. These  
309 samples are 1 GPa-treated products, and the pressure effect that they exhibit is analyzed in  
310 detail below.

311

### 312 **Cell parameter variations in relation to treatment pressure**

313 Comparison of the  $a$ ,  $b$ , and  $c$  axial lengths of sillimanite and mullite with

314 experimental pressure (Fig. 9) shows that increased pressure, but not increased temperature,  
315 caused shrinkage of the  $a$  axial length of mullite, but the  $b$  and  $c$  axial lengths did not show  
316 any remarkable change. This result is mostly consistent with the findings of Hariya et al.  
317 (1969). The  $a$  axial length of mullite is acknowledged to increase almost linearly with  
318 increases in the Al component (e.g., Cameron 1977); thus, Hariya et al. (1969) estimated  
319 the chemical composition of HP experimental samples from the relation between  $a$  axial  
320 length and pressure in analytical results for mullite obtained previously. Our results show  
321 that the  $a$  axial length in the HP samples is about intermediate between that of sillimanite  
322 and 3:2 mullite, consistent with our STEM-EDS chemical analysis results (Al/Si = 2.43(6)  
323 for S\_1400°C-1GPa-52h). As Hariya et al. (1969) pointed out, our analytical results also  
324 suggest that the SiO<sub>2</sub> component in mullite increases with increasing experimental pressure.

325

### 326 **Cell parameter relationships between sillimanite and mullite**

327 To gain an overview of cell parameter relationships between sillimanite and mullite,  
328 Hariya et al. (1969) plotted sillimanite and mullite cell parameters on the  $V$ - $a$  plane, where  
329  $a$  is  $a$  axial length and  $V$  is unit cell volume. They argued on the basis of the continuity of  
330 the plots on the  $V$ - $a$  plane that structural change is continuous between sillimanite and  
331 mullite. However, as discussed above, expansion of the  $b$  axis of sillimanite is caused by  
332 Al/Si disordering with increasing temperature, and shrinkage the  $a$  axis of mullite is caused  
333 by an increased in the SiO<sub>2</sub> component with increasing pressure. To emphasize these two  
334 factors, we projected data onto the  $b$ - $a$  plane where  $b$  is  $b$  axial length (Fig. 10). The  $b$ - $a$   
335 projection does not include information on the  $c$  axis, but  $c$  axis changes caused by



336 mullitization, Al/Si disordering in sillimanite, or changes in the  $\text{Al}_2\text{O}_3$  component of  
337 mullite are very small (Figs. 7, 9). The cell parameters of siliceous mullite obtained by the  
338 1 GPa treatments in this study do not match with those of “sillimullite” by Fischer et al.  
339 (2015) (Fig. 10). Moreover, they do not plot on the tie line connecting ordered sillimanite  
340 and mullite in the  $b$ - $a$  plane projection, whereas the cell parameters of sillimullite is on the  
341 tie line reflecting its intermediate feature in crystallography. This result suggests that the  
342 structural changes between ordered sillimanite and mullite in heat-treatment are not  
343 continuous and not via “sillimullite” structure. Instead, the plots can be divided into two  
344 groups: one group consists of phases with various  $a$  axial lengths but similar  $b$  axial lengths  
345 ( $b = \sim 7.69 \text{ \AA}$ ) (Group A), and the other consists of phases with various  $b$  axial lengths but  
346 similar  $a$  axial lengths ( $a = \sim 7.485 \text{ \AA}$ ) (Group B). Group A consists of mullite with various  
347 compositions, and Group B consists of sillimanite with various degrees of Al/Si disorder. If  
348 we extend the two lines from Group B and Group A, they cross at around  $a = \sim 7.49 \text{ \AA}$ ,  $b =$   
349  $\sim 7.69 \text{ \AA}$ ; such a crossover point implies a phase with a stoichiometric  $\text{Al}_2\text{SiO}_5$  composition  
350 and disordered Al and Si, that is, completely disordered sillimanite. However, this  
351 hypothetical phase requires at least  $T > \sim 1700 \text{ }^\circ\text{C}$  and  $P > \sim 2 \text{ GPa}$ , based on the results of  
352 this study, so it is unsurprising that this phase has never been observed, including in the  
353 present experiment.

354 In contrast to this conclusion, Hariya et al. (1969) argued that a complete solid  
355 solution series exists between sillimanite and mullite at high pressures and high  
356 temperatures. However, their result should be reconsidered in light of the resolution of the  
357 XRD system used. Inspection of the XRD patterns shown by Hariya et al. (1969) indicates

358 that the resolution of their XRD system might have been too low to distinguish between  
359 sillimanite and mullite in samples in which they coexisted. For example, they show that a  
360 sample treated at 1500 °C and 1.1 GPa for 20 h had cell parameters intermediate between  
361 those of sillimanite and mullite. In this study, however, we detected two phases: partially  
362 disordered sillimanite ( $b \approx 7.68 \text{ \AA}$ ) and siliceous mullite ( $a \approx 7.52 \text{ \AA}$ ) in a sample treated  
363 under similar experimental conditions (S\_1500°C-1.0GPa-2.5h). In Figure 10, the cell  
364 parameters of the sample of Hariya et al. (1969) plots almost on a tie line connecting our  
365 two detected phases. This result suggests that the sample of Hariya et al. (1969) might have  
366 contained both mullite and sillimanite, but they detected them as a single phase. Thus, the  
367 cell parameters that they reported are likely, in reality, to be weighted means of the cell  
368 parameters of separate sillimanite and mullite phases in the sample.

369

370

### 371 **Mullitization boundary on $P$ – $T$ diagram**

372 If there is not a complete solid solution series between sillimanite and mullite under  
373 normal geological conditions, as we assert here, a transformation boundary between them  
374 should exist on the  $P$ – $T$  diagram of the  $\text{Al}_2\text{SiO}_5$  system. To estimate the position of this  
375 boundary, we plotted the experimental results of this study and the mullitization  
376 temperature of 1200 °C at 1 atm, determined by Igami et al. (2017), on the  $P$ – $T$  diagram  
377 (Fig. 11). In addition, we re-examined representative previous heat-treatment studies.

378 Holland and Carpenter (1986), who treated sillimanite samples at 1300–1620 °C  
379 and 1.8–2.0 GPa, reported abundant APBs or APB-like defects with glass inclusions. They

380 interpreted the cause of these textures to be both continuous enrichment in  $\text{Al}_2\text{O}_3$  and Al/Si  
381 disordering. In our samples, however, similar microtextures were identified by STEM-EDS  
382 to be fine mullite, and their XRD patterns indicated that mullite formed discontinuously  
383 from sillimanite. Our results imply a compositional gap between sillimanite and mullite in  
384 the  $\text{SiO}_2$ – $\text{Al}_2\text{O}_3$  system at 1.8–2.0 GPa, different from the schematic phase diagram  
385 proposed by Holland and Carpenter (1986). We consider that the samples that they  
386 described as having abundant APBs may have started to transform to mullite (Fig. 11).

387 Raterron et al. (2000) also observed glass inclusions and dislocations in sillimanite  
388 treated at 1675 °C and 0.5–3.0 GPa, and they interpreted these textures in terms of a  
389 continuous solid-solution model between sillimanite and mullite. We agree with their  
390 conclusion that mullite has a variable composition at different pressures and temperatures,  
391 but we think that a compositional gap exists between sillimanite and mullite. The glass  
392 inclusions and other textures observed by them are similar to those observed in the present  
393 HP-samples that show peaks of both sillimanite and mullite in their XRD patterns. We infer  
394 that all of their experimental samples had started to transform to mullite (Fig. 11).

395 Navrotsky et al. (1973) measured the enthalpy of solution of heat-treated samples,  
396 and found a distinct decrement of the enthalpy of solution in samples treated at >1400 °C  
397 and 1.6–2.3 GPa, compared with unheated sillimanite. They concluded that the enthalpy  
398 change was due to Al/Si disordering in stoichiometric sillimanite, but as pointed out by  
399 Holland and Carpenter (1986), this result was more likely caused by mullitization. At  
400 experimental pressures of 1.6–2.3 GPa, 1400 °C should be in the mullitization region on the  
401 *P–T* diagram (Fig. 11).

402 The mullitization boundary estimated from our experiments is shown by a broad  
403 shaded band in Figure 11. Mullitization is a very sluggish reaction, so the  $dP/dT$  gradient  
404 may be even steeper than the indicated line because the duration of our high-pressure  
405 experiments was much shorter than that of the 1 atm experiments of Igami et al. (2017).

406 Figure 11 also shows the mullitization boundaries estimated by calorimetric studies  
407 on the  $P$ – $T$  diagram (Holm and Kleppa 1966; Weill 1966; Kiseleva et al. 1983). Although  
408 our determined boundary is closest to the result of Holm and Kleppa (1966) among the  
409 three examples, Anderson and Kleppa (1969) re-evaluated the result of Holm and Kleppa  
410 (1966) and determined it to be partly inaccurate. Thus, the consistency between our result  
411 and that of Holm and Kleppa (1966) might be of little importance. The slope of the  
412 boundary estimated by this study is steeper than that of Weill (1966) or Kiseleva et al.  
413 (1983), which may imply expansion of the mullite stability field caused by the effect of  
414 pressure-induced compositional changes. Weill (1966) and Kiseleva et al. (1983) calculated  
415 the phase boundaries for mullite with a fixed composition.

416

#### 417 **Al/Si order parameter of stoichiometric sillimanite in $P$ – $T$ diagram**

418 Our XRD results revealed that sillimanite shows a continuous increase in Al/Si  
419 disorder with increasing treatment temperatures. Igami et al. (2018a) previously determined  
420 the Al/Si order parameter  $Q$  of sillimanite in some of the studied samples. These  $Q$  values  
421 are reliable because precipitated phases (mullite and glasses) were surely excluded from the  
422 analytical regions examined by TEM. In addition, our XRD results show that the pressure  
423 effect on the  $Q$  value may be negligible (Fig. 7). In Figure 12, we show  $Q$  values of

424 sillimanite as a contour on a  $P$ - $T$  diagram, where the  $Q$  values are expressed by the  
425 Bragg-Williams model as a function of temperature and independent of pressure:  $Q(T_c/T) =$   
426  $1/2 \ln[(1 + Q) / (1 - Q)]$ , where  $T_c = 1727$  °C (Igami et al. 2018a). Thus, the  $Q$  contour line  
427 is projected vertically onto the  $P$ - $T$  plane.

428 This figure shows that the  $Q$  value at the aluminosilicate triple point is much higher  
429 than  $Q = 0.975$ . Similarly, the  $Q$  value at the sillimanite–andalusite boundary is higher than  
430  $\sim 0.95$ . Therefore, the effect of Al/Si disordering on the triple point equilibrium and the  
431 sillimanite–andalusite boundary seem to be negligible. In contrast, the sillimanite on the  
432 sillimanite–kyanite boundary at high temperatures is in a relatively low ordered state,  
433 which indicates that the stability field of sillimanite should expand toward that of kyanite.  
434 These results agree with the conclusions of previous theoretical studies (e.g., Saxena 1974).

435

436

### Implications

437 The present experimental results imply that submicrometric textures and  
438 crystallographic features of sillimanite and mullite may be useful for investigating the  
439 thermal history of natural samples, in particular, rocks produced by ultra-high-temperature  
440 metamorphism.

441 For example, Aramaki (1961) reported that sillimanite in pelitic xenoliths from  
442 Asama Volcano in Japan have cell parameters  $a = 7.498(3)$ ,  $b = 7.690(3)$ , and  $c = 5.797(3)$   
443 Å, which are near the crossover point shown in Figure 10. Cameron and Ashworth (1972)  
444 studied the same Asama sillimanite and reported slightly different cell parameters:  $a =$   
445  $7.4963(4)$ ,  $b = 7.6851(4)$ , and  $c = 5.7764(3)$  Å. Recently, we showed that mullite with a

446 submicrometric core-rim texture coexists with sillimanite in aluminosilicates from the same  
447 locality (Igami et al. 2018b); thus, the previously reported cell parameters can be  
448 interpreted as resulting from the presences of double sillimanite and mullite peaks, similar  
449 to our interpretation of the results of Hariya et al. (1969). Under this assumption, the *b* axial  
450 length of sillimanite reported by Cameron and Ashworth (1972) seems to be rather large, an  
451 indication that the Al/Si arrangement is considerably disordered. This finding is consistent  
452 with the TEM observation of Igami et al. (2018b) that APBs with a displacement vector of  
453  $1/2[001]$  were abundant in the sample. The cell parameters reported by Aramaki (1961)  
454 have no clear explanation, but their differences with those reported by Cameron and  
455 Ashworth (1972) probably reflect a difference in the abundance ratio of sillimanite and  
456 mullite. Although the low Al/Si order parameter of this sillimanite cannot be directly  
457 associated with temperature in Figure 12, because this low ordered state was probably  
458 caused by the transformation of mullite to sillimanite (Igami et al. 2018b), the sample might  
459 have reached temperatures around the mullitization boundary.

460 As in the case of this Asama aluminosilicate example, many interesting  
461 characteristics of sillimanite and mullite samples may be overlooked. Investigations of  
462 sillimanite that take account of the results of this study can yield new information about  
463 thermal histories in high-temperature regions above 1000 °C that is easy to be lost in  
464 general.

465

466

467

## Acknowledgments

468           We are grateful to Akira Tsuchiyama, Norimasa Shimobayashi, Takao Hirajima,  
469 Tetsuo Kawakami, and Masao Kitamura for critical discussions. We sincerely thank  
470 Toshiyuki Kawasaki for providing the samples. We also thank Yu Kodama, Tatsuya Osako  
471 Yuh-Chyuan Chang, and Tomoki Taguchi for their help with the experiments conducted at  
472 the Photon Factory. This manuscript was greatly improved by outstanding comments by  
473 Reinhard X. Fischer and an anonymous reviewer. This work was supported by JSPS  
474 KAKENHI Grant Number JP16H06348 to AM.  
475

476

## References

- 477 Anderson, P.A.M., and Kleppa, O.J. (1969) The thermochemistry of the kyanite-sillimanite  
478 equilibrium. *American Journal of Science*, 267, 285–290.
- 479 Aramaki, S. (1961) Sillimanite and cordierite from volcanic xenoliths. *American*  
480 *Mineralogist*, 46, 1154–1165.
- 481 Bish, D.L., and Burnham, G.W. (1992) Rietveld refinement of the crystal structure of  
482 fibrolitic sillimanite using neutron powder diffraction data. *American Mineralogist*,  
483 77, 374–379.
- 484 Burnham, C.W. (1963) Refinement of the crystal structure of sillimanite. *Zeitschrift für*  
485 *Kristallographie*, 118, 127–148.
- 486 Cameron, W.E. (1977) Mullite; a substituted alumina. *American Mineralogist*, 62, 747–755.
- 487 Cameron, W.E., and Ashworth, J.R. (1972) Fibrolite and its relationship to sillimanite.  
488 *Nature Physical Science*, 235, 134.
- 489 Fischer, R.X., Gaede-Köhler, A., Birkenstock, J., and Schneider, H. (2012) Mullite and  
490 mullite-type crystal structures. *International Journal of Materials Research*, 103,  
491 402–407.
- 492 Fischer, R.X., Tikhonova, V., Birkenstock, J., Fischer, L.A., Herrmann, K., Mengel, K., and  
493 Schneider, H. (2015). A new mineral from the Bellerberg, Eifel, Germany,  
494 intermediate between mullite and sillimanite. *American Mineralogist*, 100,  
495 1493–1501.
- 496 Greenwood, H.J. (1972) Al<sup>IV</sup>-Si<sup>IV</sup> disorder in sillimanite and its effect on phase relations  
497 of the aluminum silicate minerals. *Geological Society of America, Memoir*, 132,



- 498           553–571.
- 499   Hariya, Y., Dollase, W.A., and Kennedy, G.C. (1969) An experimental investigation of the  
500           relationship of mullite to sillimanite. *American Mineralogist*, 54, 1419–1441.
- 501   Holdaway, M.J. (1971) Stability of andalusite and the aluminum silicate phase diagram.  
502           *American journal of science*, 271, 97–131.
- 503   Holland, T.J.B., and Carpenter, M.A. (1986) Aluminium/ silicon disordering and melting in  
504           sillimanite at high pressures. *Nature*, 320, 151–153.
- 505   Holm, J.L., and Kleppa, O.J. (1966) The thermodynamic properties of the aluminum  
506           silicates. *American mineralogist*, 51, 1608–1622.
- 507   Ida, T. (2005) Connection of segmented intensity data measured with a multiple-detector  
508           system for powder diffractometry. *Journal of Applied Crystallography*, 38, 795–803.
- 509   Ida, T., Hibino, H., and Toraya, H. (2003) Deconvolution of instrumental aberrations for  
510           synchrotron powder X-ray diffractometry. *Journal of Applied Crystallography*, 36,  
511           181–187.
- 512   Igami, Y., Ohi, S., and Miyake, A. (2017) Sillimanite–mullite transformation observed in  
513           synchrotron X-ray diffraction experiments. *Journal of the American Ceramic*  
514           *Society*, 100, 4928–4937.
- 515   Igami, Y., Kuribayashi, T., and Miyake, A. (2018a) Determination of Al/Si order in  
516           sillimanite by high angular resolution electron channeling X-ray spectroscopy, and  
517           implications for determining peak temperatures of sillimanite. *American*  
518           *mineralogist*, 103, 944–951.
- 519   Igami, Y., Miyake, A., and Shimobayashi, N. (2018b) Mullite in a buchite from Asama

- 520 volcano and its sub-micrometric core-rim texture with sillimanite. Journal of  
521 Mineralogical and Petrological Sciences, 113, 198–206.
- 522 Kawasaki, T., Ishikawa, M., and Motoyoshi, Y. (1993) A preliminary report on  
523 cordierite-bearing assemblages from Rundvågshetta, Lützow-Holm Bay, East  
524 Antarctica: Evidence for a decompressional *P-T* path? Proceedings of NIPR  
525 Symposium of Antarctic Geosciences, 6, 47–56.
- 526 Kawasaki, T., Nakano, N., and Osanai, Y. (2011) Osumilite and a spinel + quartz  
527 association in garnet–sillimanite gneiss from Rundvågshetta, Lützow-Holm  
528 Complex, East Antarctica. Gondwana Research, 19, 430–445.
- 529 Kiseleva, I.A., Ostapenko, G.T., Ogorodova, L.P., Topor, N.D., and Timoshkova, L.P.  
530 (1983) High-temperature calorimetry data on the equilibrium between andalusite,  
531 kyanite, sillimanite, and mullite. Geochemistry International, 20, 17–26.
- 532 Machida, S., Kogiso, T., and Hirano, N. (2017) Petit-spot as definitive evidence for partial  
533 melting in the asthenosphere caused by CO<sub>2</sub>. Nature Communications, 8, 14302.
- 534 Navrotsky, A., Newton, R.C., and Kleppa, O.J. (1973) Sillimanite-disordering enthalpy by  
535 calorimetry. Geochimica et Cosmochimica Acta, 37, 2497–2508.
- 536 Peterson, R.C., and McMullan, R.K. (1986) Neutron diffraction studies of sillimanite.  
537 American Mineralogist, 71, 742–745.
- 538 Raterron, P., Carpenter, M., and Doukhan, J.C. (1999) Sillimanite mullitization: ATEM  
539 investigation and point defect model. Phase transitions, 68, 451–500.
- 540 Raterron, P., Carpenter, M., and Doukhan, J.C. (2000) ATEM investigation of  
541 experimentally annealed sillimanite: new constraints for the SiO<sub>2</sub> - Al<sub>2</sub>O<sub>3</sub> join.

- 542 Mineralogical Magazine, 64, 247–254.
- 543 Saxena, S.K. (1974) Order disorder in sillimanite. Contributions to Mineralogy and  
544 Petrology, 45, 161–167.
- 545 Toraya, H., Hibino, H., and Ohsumi, K. (1996) A new powder diffractometer for  
546 synchrotron radiation with a multiple-detector system. Journal of Synchrotron  
547 Radiation, 3, 75–83.
- 548 Weill, D.F. (1966) Stability relations in the  $\text{Al}_2\text{O}_3$ – $\text{SiO}_2$  system calculated from solubilities  
549 in the  $\text{Al}_2\text{O}_3$ – $\text{SiO}_2$ – $\text{Na}_3\text{AlF}_6$  system. Geochimica et Cosmochimica Acta, 30,  
550 223–237.
- 551 Winter, J.K., and Ghose, S. (1979) Thermal expansion and high-temperature crystal  
552 chemistry of the  $\text{Al}_2\text{SiO}_5$  polymorphs. American Mineralogist, 64, 573–586.
- 553 Zen, E.A. (1969) The stability relations of the polymorphs of aluminum silicate; a survey  
554 and some comments. American Journal of Science, 267, 297–309.
- 555

556 **Table titles and figure captions**

557

558 **Tables**

559 Table 1.

560 Cell parameters of detected crystalline phases in the experimental samples at 1 atm.

561

562 Table 2.

563 Cell parameters of detected crystalline phases in the experimental samples at high  
564 pressures.

565

566 Table 3.

567 TEM observation results.

568

569 **Figures**

570 **Figure 1.**

571 Powder X-ray diffraction patterns of STR (lower) and S<sub>1476°C-1atm-10h</sub> (upper). **(a)**  
572 Whole diffraction patterns. All the peaks in STR are reflections of sillimanite. The label of  
573 “Sil 210” indicates 210 reflection of sillimanite, which is enlarged in Figure 2. **(b)(c)**  
574 Enlargements of representative peaks. The reflections of 121, 211 and 220 of sillimanite are  
575 shown from both STR and S<sub>1476°C-1atm-10h</sub> (solid arrows). On the assumption that the  
576 space group of the new appeared phase is *Pbnm* same with sillimanite, 121, 211 and 220  
577 reflection peaks are predicted to appear at  $2\theta = 34.51, 34.83$  and  $37.88^\circ$ , respectively

578 (dotted arrows). In the pattern of S\_1476°C-1atm-10h, there are a clear peak  
579 corresponding to 220 reflection (c), but no peak corresponding to 121 or 211 which is the  $l$   
580 = odd reflections (b).

581

582 **Figure 2.**

583 XRD peak shifts induced by (a) high temperature and (b) high temperature and high  
584 pressure treatments. The peaks are labeled with their Miller indices, preceded by sil for  
585 sillimanite and mul for mullite. (a) XRD patterns of STR, S\_1000°C-1atm-700h,  
586 S\_1090°C-1atm-1255h, S\_1200°C-1atm-500h, S\_1290°C-1atm-60h,  
587 S\_1373°C-1atm-1711h, and S\_1476°C-1atm-10h, arranged in order of treatment  
588 temperature. (b) XRD patterns of 1373°C-1atm-300h, 1400°C-0.2GPa-19h, and  
589 1400°C-1.0GPa-2.5h, arranged in order of treatment pressure.

590

591 **Figure 3.**

592 TEM images and SAED patterns of S\_1476°C-1atm-696h. (a) BF-TEM image and SAED  
593 pattern on the projection of [100]. In case of indexing using sillimanite cell parameters, the  
594  $l = \text{odd}$  reflections are extinct, which means the samples completely transformation to  
595 mullite. (b) BF-TEM image and SAED patterns on the projection of [001]. SAED pattern  
596 taken from an inclusion (lower right), shows glass halo.

597

598 **Figure 4.**

599 S/TEM-EDS images of S\_1450°C-1atm-1150h. (a) DF-TEM image of the section taken

600 from the  $g = 101$  reflection of sillimanite. **(b)** SAED pattern of the same area. **(c)**  
601 ADF-STEM images. **(d)** X-ray map obtained by dividing  $I_{Al-K}$  by  $I_{Si-K}$ .

602

603 **Figure 5.**

604 S/TEM-EDS images of S\_1373°C-1atm-300h. **(a)** BF-TEM image and **(b)** DF-TEM image  
605 taken from the  $g = 021$  reflection. **(c)** SAED pattern of the same area. **(d)** ADF-STEM  
606 image. **(e)** X-ray map obtained by dividing  $I_{Al-K}$  by  $I_{Si-K}$ .

607

608 **Figure 6.**

609 TEM images and SAED patterns of S\_1400°C-1GPa-52h. **(a)** BF-TEM image of a section  
610 containing two grains. **(b)** Enlarged BF-TEM image of the region enclosed by a dotted  
611 rectangle in (a) and the SAED pattern of the same area, which shows a mullite pattern.  
612 There are fewer glass inclusions than in the samples heat treated at 1 atm. **(c)** Enlarged BF-  
613 and DF-TEM images of the region enclosed by a second dotted rectangle in (a) and the  
614 SAED pattern of the same area. The SAED pattern shows the  $l = \text{odd}$  reflections of  
615 sillimanite, and the DF image is taken from the  $g = 211$  reflection of sillimanite. In this  
616 grain, an APB-like texture with few glass inclusions was observed.

617

618 **Figure 7.**

619 **(a)**  $a$ , **(b)**  $b$ , and **(c)**  $c$  axial lengths of sillimanite and mullite in relation to treatment  
620 temperature. To simplify comparison with sillimanite, the  $c$  axis of mullite is treated as the  
621 twice length. The panels on the right are enlargements of the areas between the dashed

622 horizontal lines in the left panels. Arrows in the left panel of (a) indicate mullite in the 1  
623 GPa treatment product.

624

625 **Figure 8.**

626 Order parameter  $Q$  values from Igami et al. (2018a) plotted against  $b$  axial lengths  
627 determined in this study;  $Q$  and  $b$  tend to be negatively correlated.

628

629 **Figure 9.**

630 (a)  $a$ , (b)  $b$ , and (c)  $c$  axial lengths of sillimanite and mullite plotted against experimental  
631 pressure.

632

633 **Figure 10.**

634 Projection of our results on the  $b$ - $a$  plane. A continuous relationship between ordered  
635 sillimanite and mullite is not observed. Instead, the plots can be divided into Group A and  
636 Group B with a hypothetical crossover point at  $a = \sim 7.49 \text{ \AA}$ ,  $b = \sim 7.69 \text{ \AA}$ . The  
637 1500°C-1.1GPa-20h product reported by Hariya et al. (1969) (rhombus), lies roughly on the  
638 tie line (dotted line) between the two phases that we detected in a similar experimental  
639 sample in this study (S\_1500°C-1.0GPa-2.5h, shown by large circle and large square). If  
640 we assume that the cell parameters of Asama sillimanite (Cameron and Ashworth 1972) are  
641 weighted means of sillimanite and mullite parameters, then the  $b$  axial length of sillimanite  
642 seems to be relatively large compared with the STR of this study, indicating a disordered  
643 Al/Si arrangement.

644

645 **Figure 11.**

646 *P–T* diagram showing the phase relation between sillimanite and mullite in the results of  
647 this study and previous studies. In this study, open circles indicate that mullite is present,  
648 and filled circles indicate that it is absent. Half-filled circles indicate that presence of  
649 mullite is slight or unclear. The mullitization temperature at 1 atm (1200 °C) determined by  
650 reaction kinetics analysis (Igami et al., 2017) is plotted by a cross. Previous studies reported  
651 that some experimentally heated samples show intermediate feature between sillimanite and  
652 mullite (hatched symbols), but their samples may have coexistence of mullite and  
653 sillimanite, according to comparison of the original description with our results. The broad  
654 shaded band shows the mullitization boundary estimated in this study. Mullitization  
655 boundaries estimated by previous studies are also shown.

656

657 **Figure 12.**

658 *P–T* diagram of the  $\text{Al}_2\text{SiO}_5$  system showing the contour of the  $Q$  value of sillimanite.  
659 Phase boundaries between kyanite, andalusite, and sillimanite follow Holdaway (1971).  
660 The  $Q$  values are expressed as a function of temperature, and independent of pressure, in  
661 accordance with the Bragg-Williams model (Igami et al. 2018a):  $Q(T/T_c) = 1/2 \ln[(1 + Q) /$   
662  $(1 - Q)]$ , where  $T_c = 1727$  °C. The stability field of sillimanite should expand toward that of  
663 kyanite with increasing temperature because of Al/Si disordering (expressed schematically  
664 by the curved dashed line).

665



Sample Name	Sillimanite			Mullite		
	<i>a</i> (Å)	<i>b</i> (Å)	<i>c</i> (Å)	<i>a</i> (Å)	<i>b</i> (Å)	<i>c</i> (Å)
S_790°C-1atm-700h	7.4850(3)	7.6742(2)	5.7719(3)	-	-	-
S_890°C-1atm-700h	7.4855(2)	7.67446(1 3)	5.7724(2)	-	-	-
S_1000°C-1atm-700h	7.4859(2)	7.67446(1 2)	5.7722(2)	Δ	Δ	Δ
S_1040°C-1atm-700h	7.4858(2)	7.67490(1 1)	5.7722(2)	Δ	Δ	Δ
S_1090°C-1atm-1255h	7.4861(2)	7.67497(1 3)	5.7720(2)	Δ	Δ	Δ
S_1140°C-1atm-1512h	7.4867(2)	7.67586(1 1)	5.7722(2)	Δ	Δ	Δ
S_1200°C-1atm-500h	7.4861(2)	7.67566(1 5)	5.7717(2)	Δ	Δ	Δ
S_1240°C-1atm-144h	7.4869(2)	7.67642(1 2)	5.7717(2)	Δ	Δ	Δ
S_1239°C-1atm-785h	7.4877(2)	7.67672(1 3)	5.7720(3)	7.5403(6)	7.6880(9)	2.8852(6)
S_1290°C-1atm-60h	7.4865(2)	7.67698(1 3)	5.7717(2)	7.5513(10 )	7.6923(8)	2.8867(8)
S_1373°C-1atm-70h	7.4874(2)	7.6788(2)	5.7711(2)	7.5441(5)	7.6905(3)	2.8846(3)
S_1373°C-1atm-300h	7.4873(2)	7.67968(1 3)	5.7718(2)	7.5423(4)	7.6916(2)	2.8855(2)
S_1373°C-1atm-1711h	7.4884(2)	7.6809(2)	5.7717(3)	7.5385(4)	7.6912(3)	2.8852(2)
S_1476°C-1atm-1h	7.4873(2)	7.6810(2)	5.7713(2)	7.5480(4)	7.6889(6)	2.8853(4)
S_1476°C-1atm-10h	7.4886(2)	7.68245(1 2)	5.7719(2)	7.5390(5)	7.6914(3)	2.8858(3)
S_1476°C-1atm-90h	7.4903(4)	7.6835(3)	5.7707(5)	7.5440(2)	7.69141(15 )	2.88502(11)
S_1476°C-1atm-696h	-	-	-	7.5408(2)	7.6919(2)	2.88457(11)
S_1530°C-1atm-5h	7.4879(2)	7.6828(2)	5.7712(2)	7.5496(3)	7.6888(3)	2.8853(2)
S_1530°C-1atm-20h	7.4898(3)	7.6854(3)	5.7714(3)	7.5484(4)	7.6902(3)	2.8856(2)
S_1530°C-1atm-60h	-	-	-	7.5436(5)	7.6927(3)	2.8848(3)

Note: ○, detected; Δ, slightly detected; -, not detected

---

Corundum

---

-

-

-

-

-

-

-

-

-

-

-

-

-

-

-

-

-

-

---

Sample Name	Sillimanite			Mullite		
	<i>a</i> (Å)	<i>b</i> (Å)	<i>c</i> (Å)	<i>a</i> (Å)	<i>b</i> (Å)	<i>c</i> (Å)
S_1200°C-0.2GPa-45h	7.4869(2)	7.67690(13)	5.7714(2)	△	△	△
S_1300°C-0.2GPa-41.5h	7.4882(2)	7.6799(2)	5.7710(3)	7.5374(7)	7.6887(5)	2.8856(5)
S_1400°C-0.2GPa-19h	7.4884(2)	7.68184(11)	5.7703(3)	7.5401(6)	7.6894(5)	2.8833(5)
S_1400°C-1GPa-2.5h	7.4866(2)	7.68184(13)	5.7701(4)	7.5200(3)	7.6906(2)	2.8840(3)
S_1500°C-1GPa-2.5h	7.4874(2)	7.68280(14)	5.7700(4)	7.5219(5)	7.6901(3)	2.8843(5)
S_1300°C-2.5GPa-24h	7.48767(15)	7.67745(11)	5.7717(2)	-	-	-
S_1400°C-2.4GPa-22h	7.4913(2)	7.6806(2)	5.7716(2)	-	-	-

Note: ○, detected; △, slightly detected; -, not detected

---

Corundum

---

○

○

○

-

-

○

○

---

Sample name (Section No.)	Glass inclusion	APB-like texture	Mullite region
S_1530°C-1 atm-5h (1)	⊙	⊙	○
S_1476°C-1 atm-696h (1)	⊙	-	⊙
S_1476°C-1 atm-90h (1)	⊙	-	⊙
S_1476°C-1 atm-10h (1)	⊙	⊙	○
S_1476°C-1 atm-1h (1)	○	○	○
S_1476°C-1 atm-1h (2)	○	○	-
S_1450°C-1 atm-1150h (1)	⊙	⊙	⊙
S_1373°C-1 atm-1711h (1)	○	○	-
S_1373°C-1 atm-1711h (2)	⊙	⊙	-
S_1373°C-1 atm-300h (1)	⊙	⊙	-
S_1373°C-1 atm-300h (2)	○	△	-
S_1373°C-1 atm-300h (3)	-	-	-
S_1373°C-1 atm-70h (1)	△	△	-
S_1290°C-1 atm-60h (1)	○	○	-
S_1290°C-1 atm-60h (2)	○	-	○
S_1239°C-1 atm-785h (1)	△	△	-
S_1140°C-1 atm-1512h (1)	-	-	-
S_1140°C-1 atm-1512h (2)	-	-	-
S_1140°C-1 atm-1512h (3)	-	-	-
S_1090°C-1 atm-1255h (1)	-	-	-
S_1400°C-0.2 GPa-19h (1)	⊙	⊙	-
S_1400°C-1.0 GPa-52h (1)	△	○	⊙
S_1400°C-2.4 GPa-22h (1)	-	○	-
S_1400°C-2.4 GPa-22h (2)	△	○	-

S_1400°C-2.4 GPa-22h (3)	△	-	-
Starting material (1)	-	-	-
Starting material (2)	-	-	-

Note: ⊙, abundantly observed; ○, observed; △, rarely observed; -, never

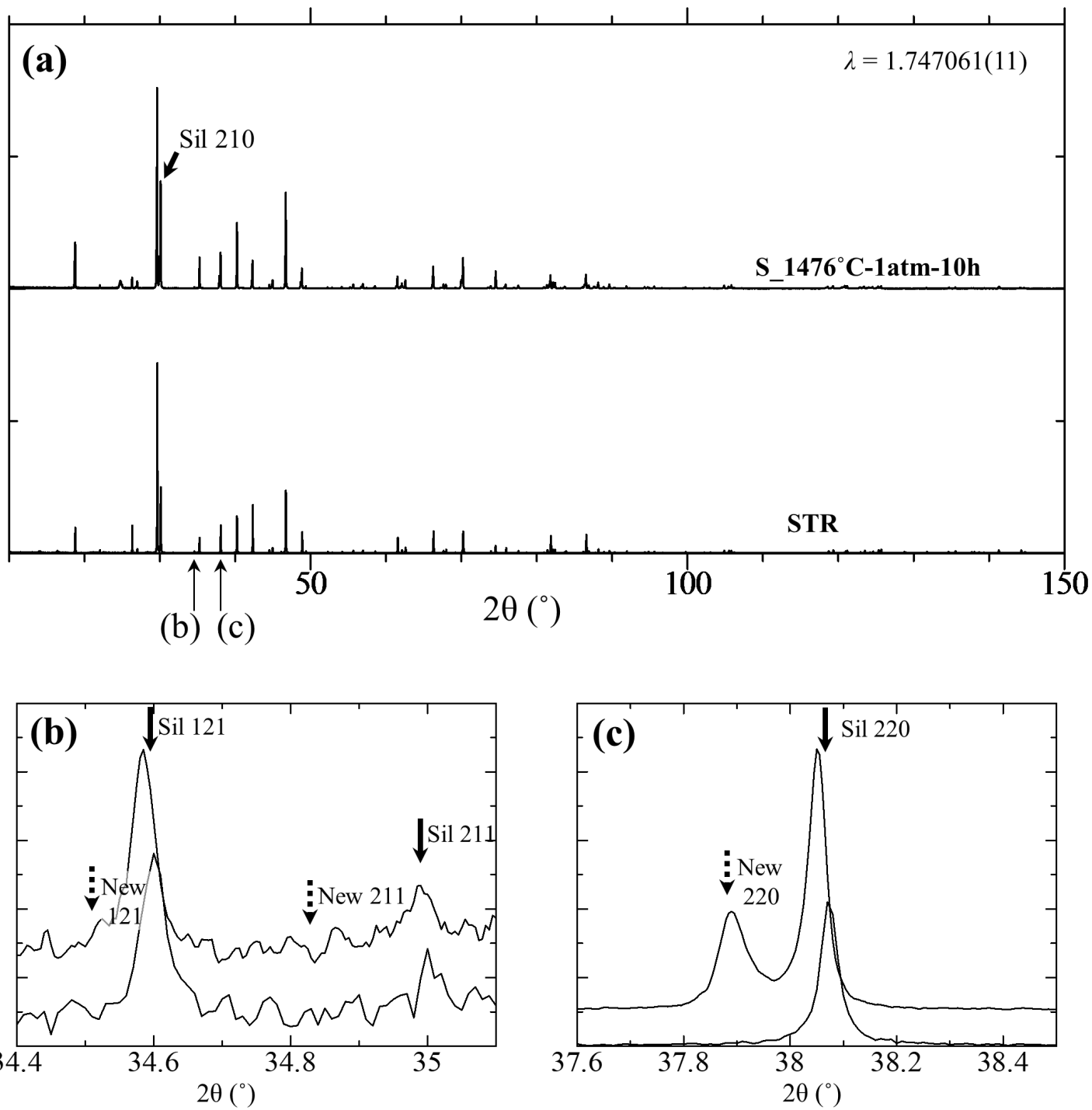


Figure 1

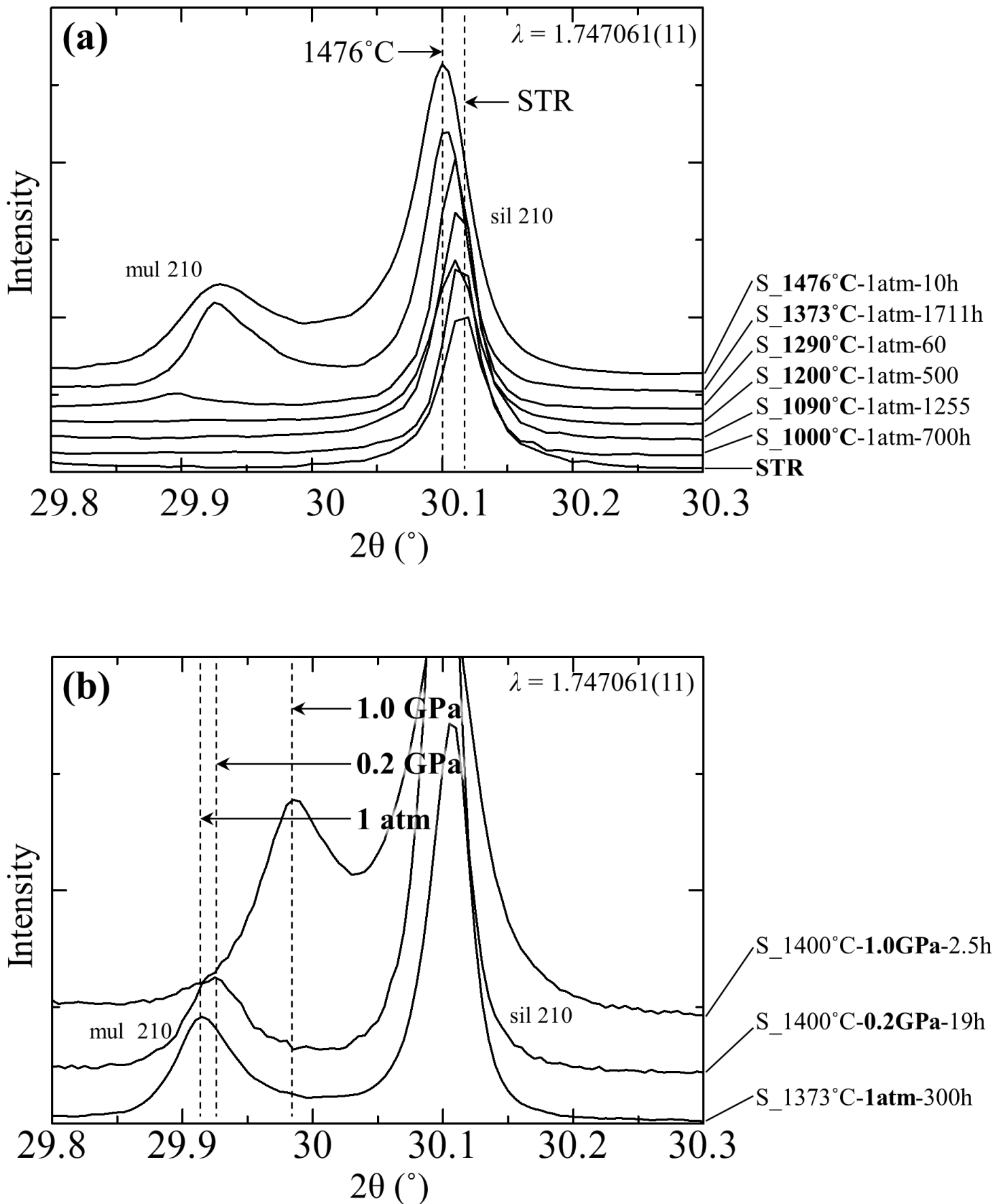


Figure 2



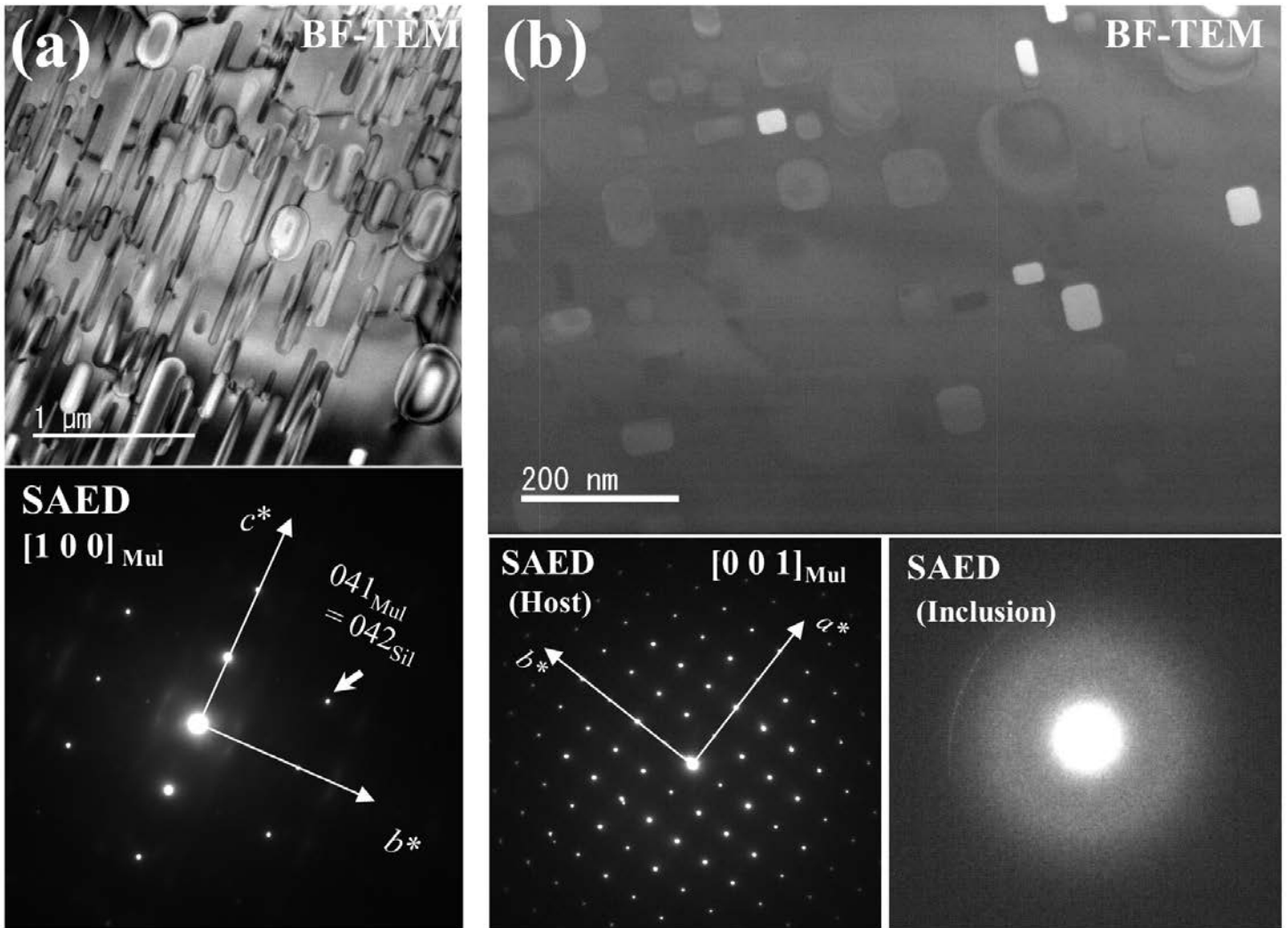


Figure 3

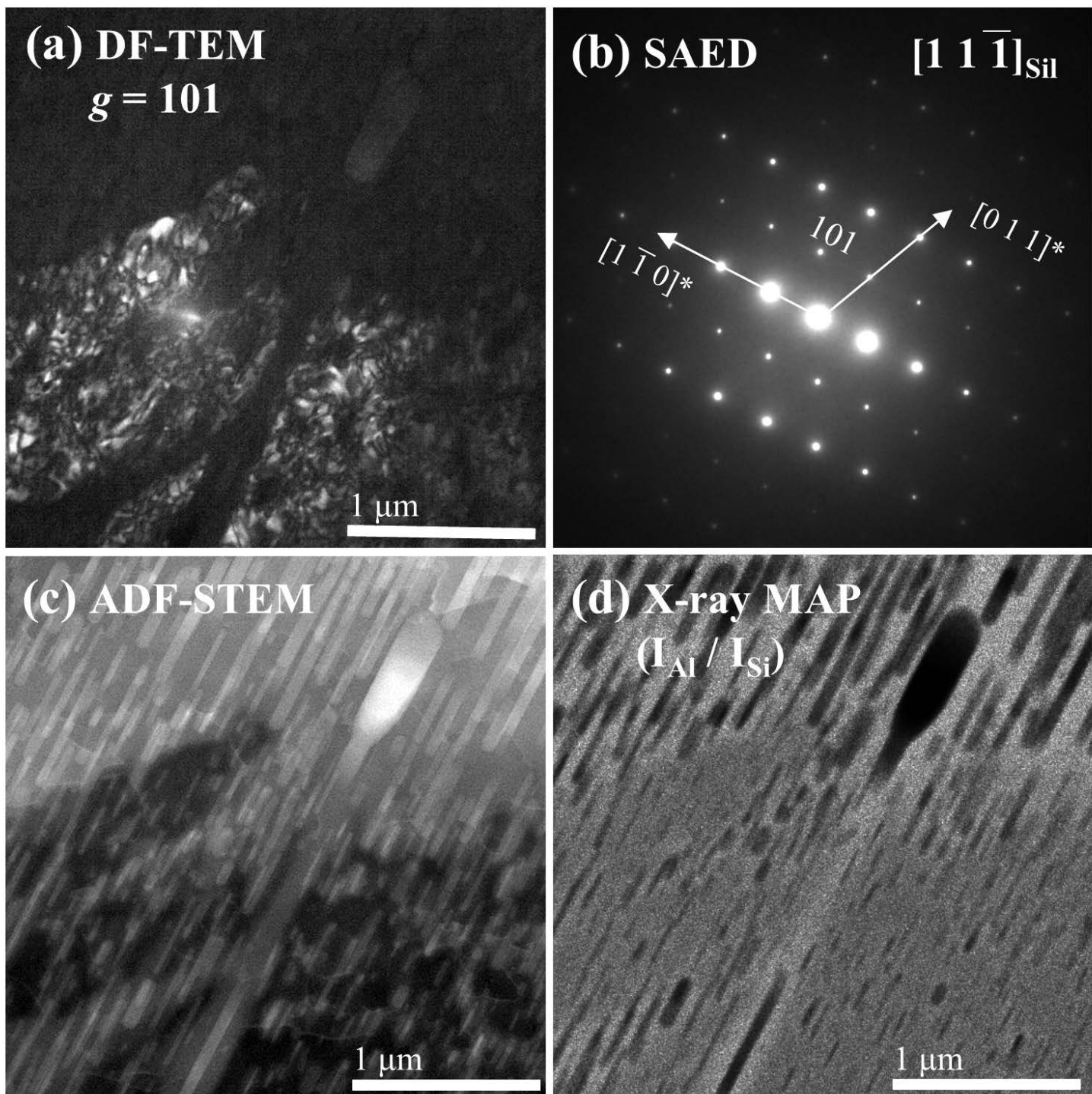


Figure 4

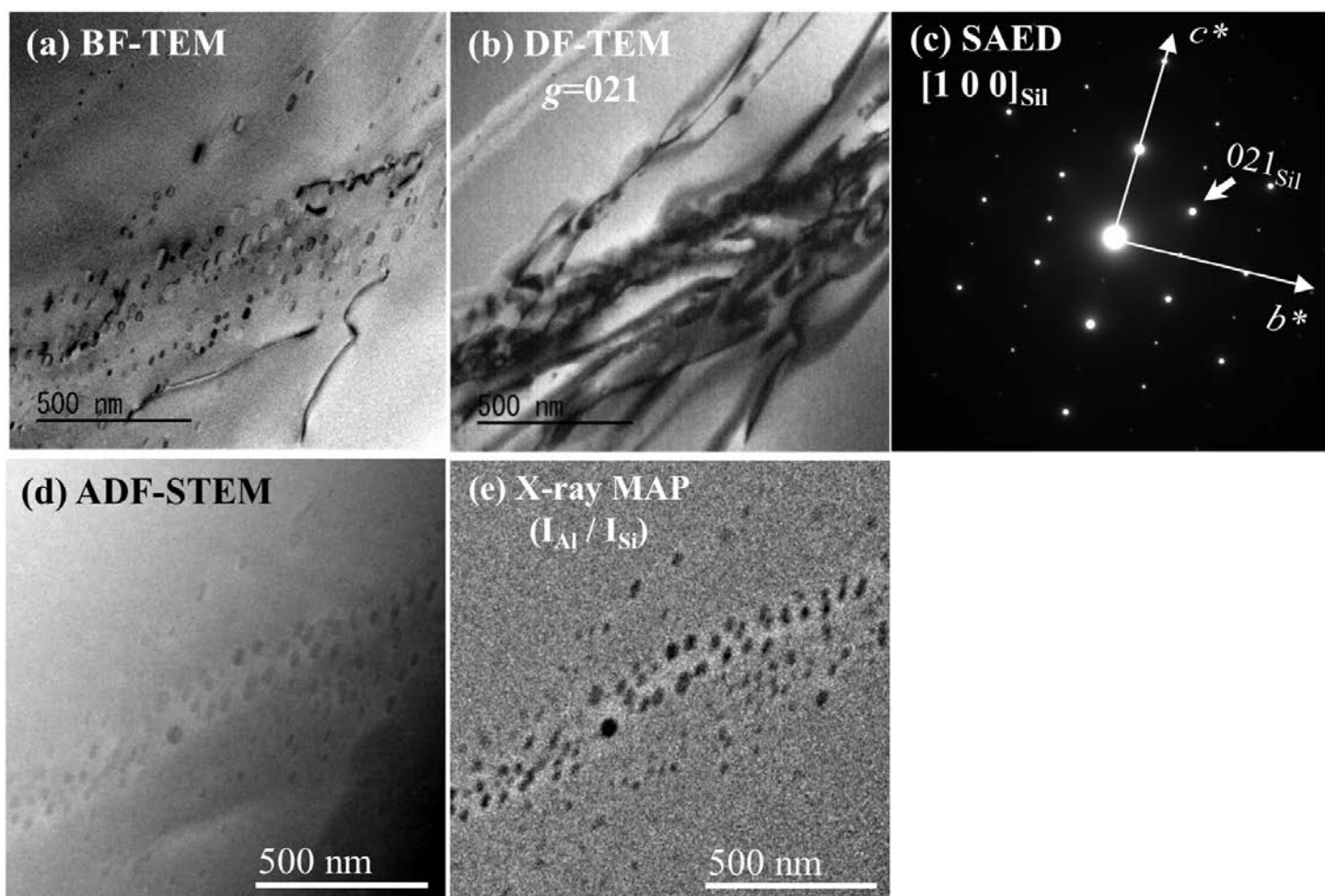


Figure 5

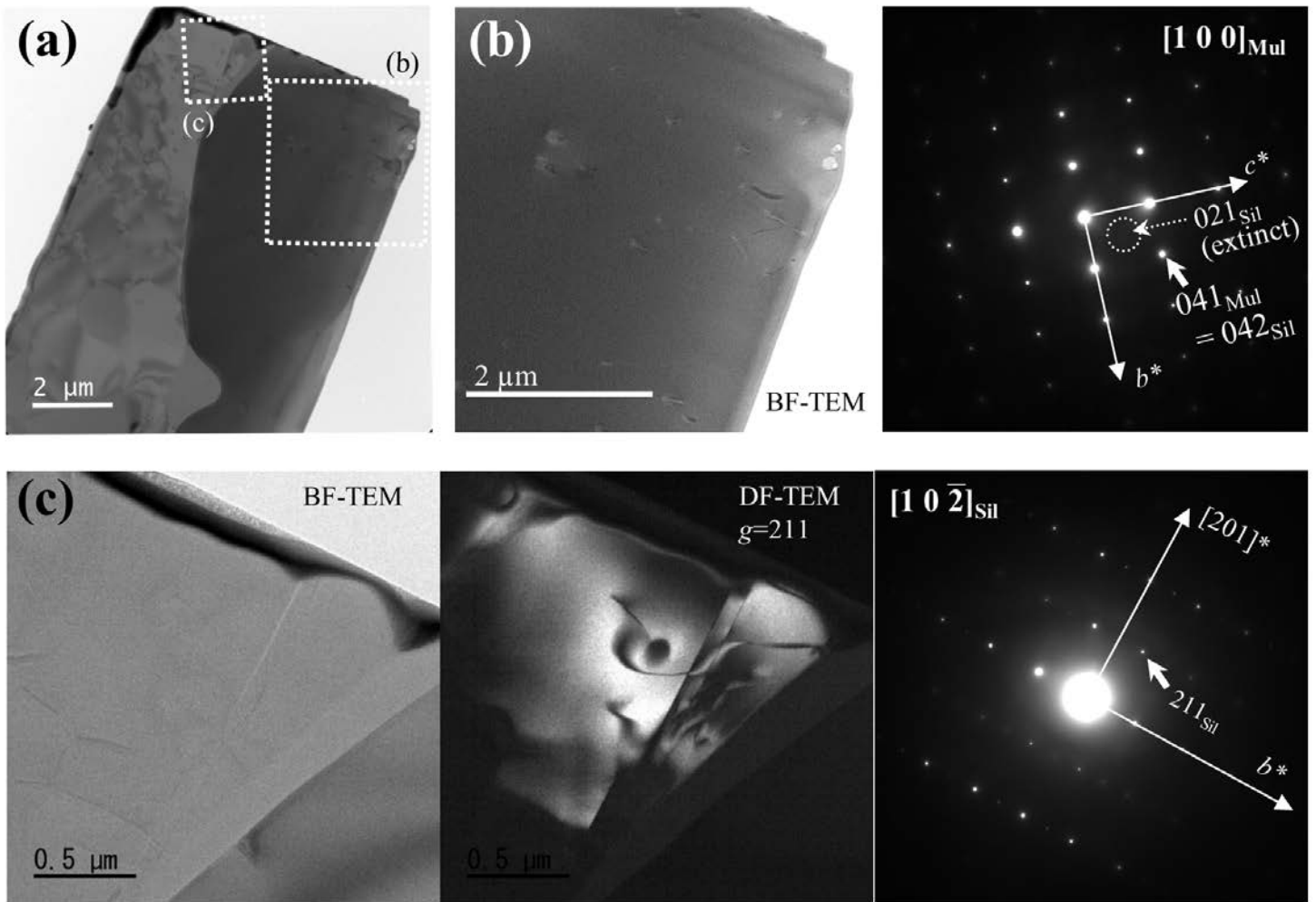


Figure 6

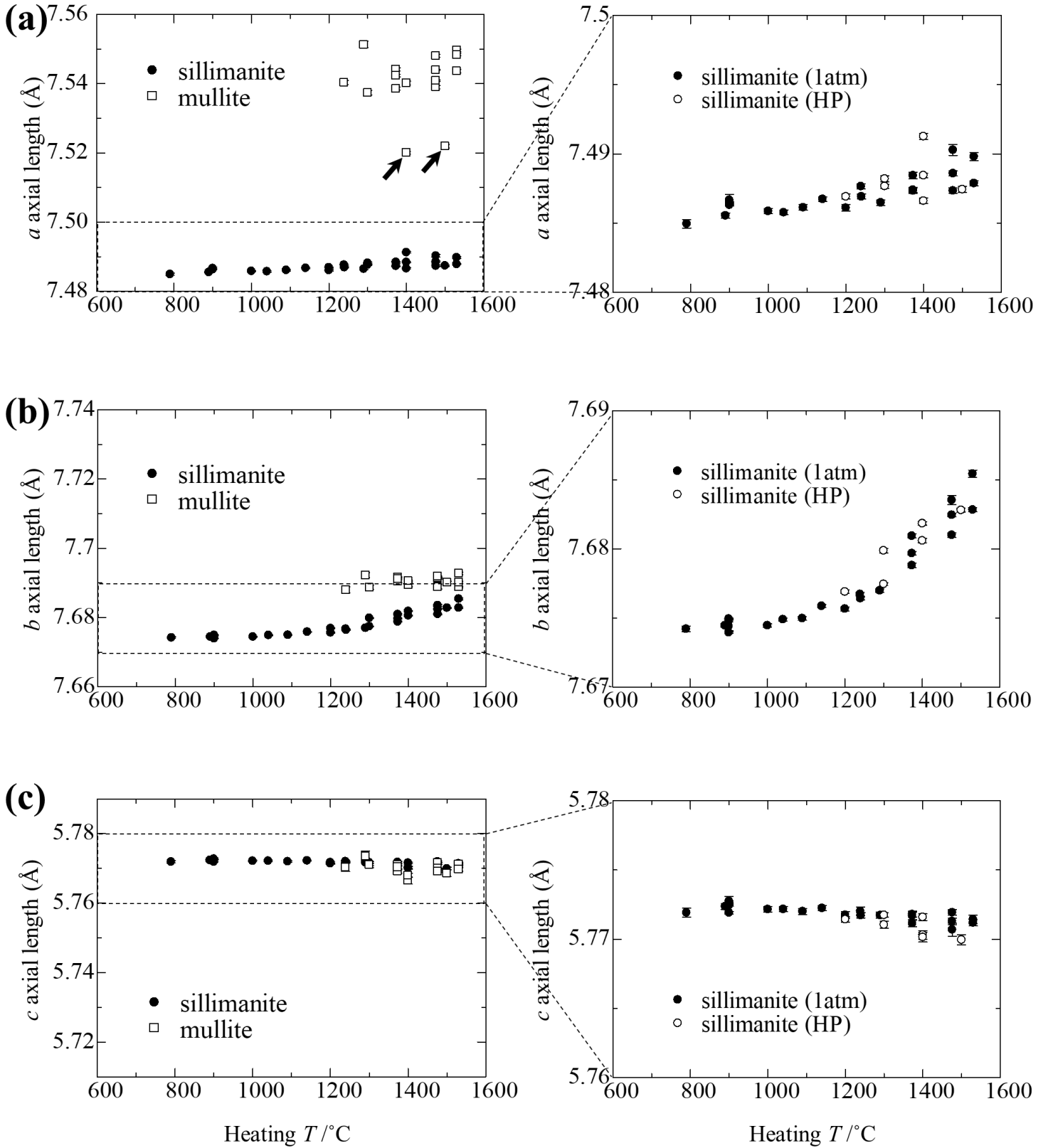


Figure 7

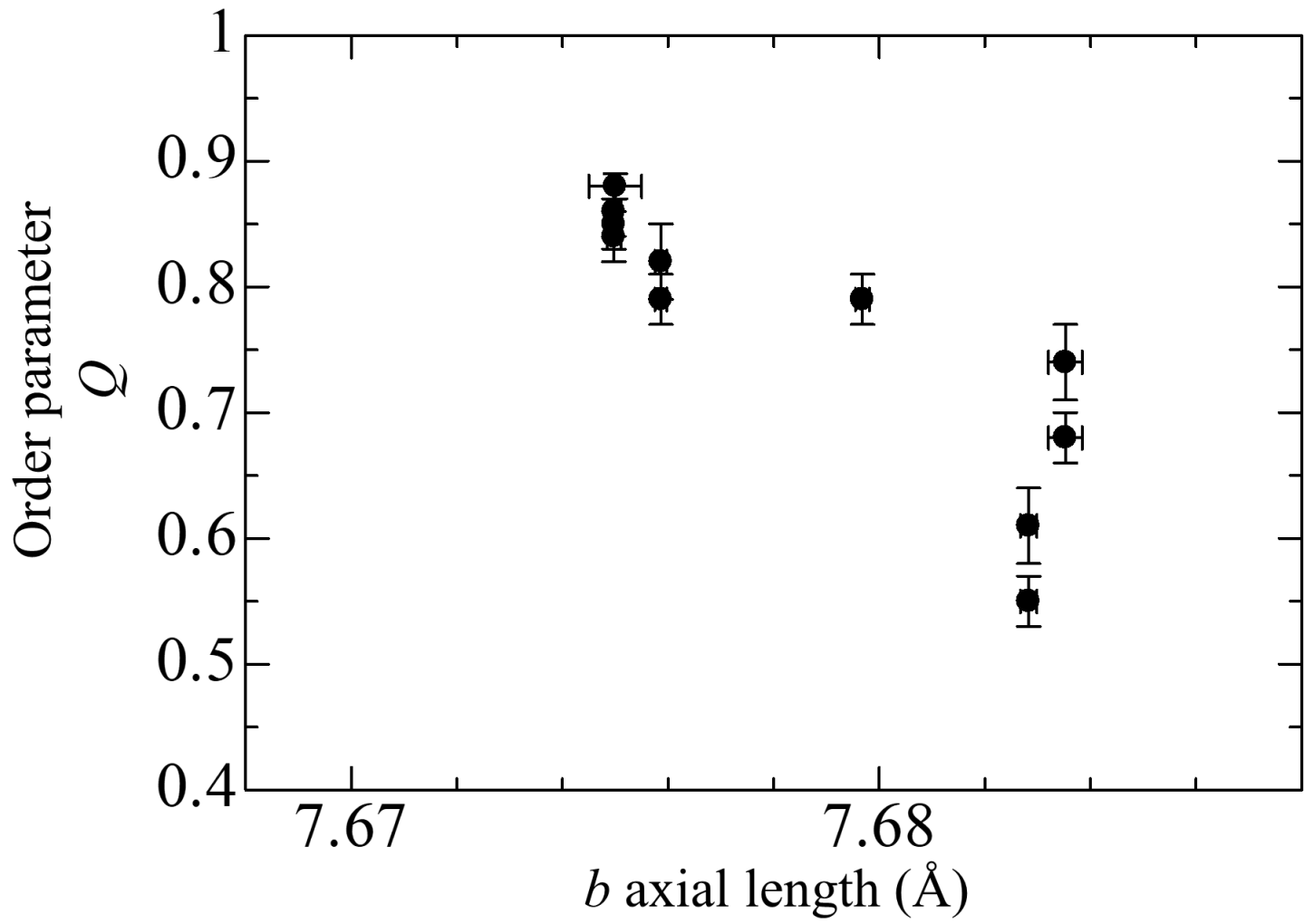


Figure 8

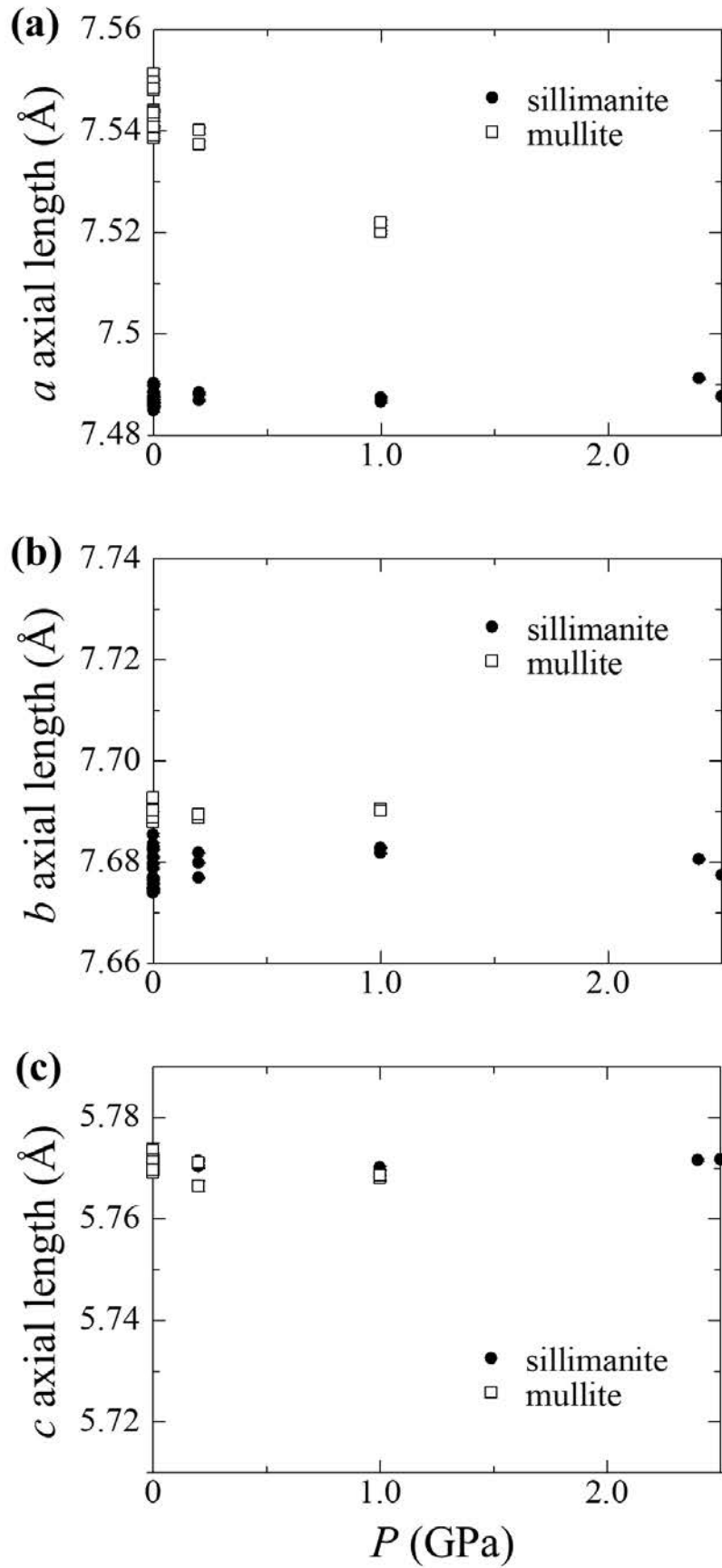


Figure 9

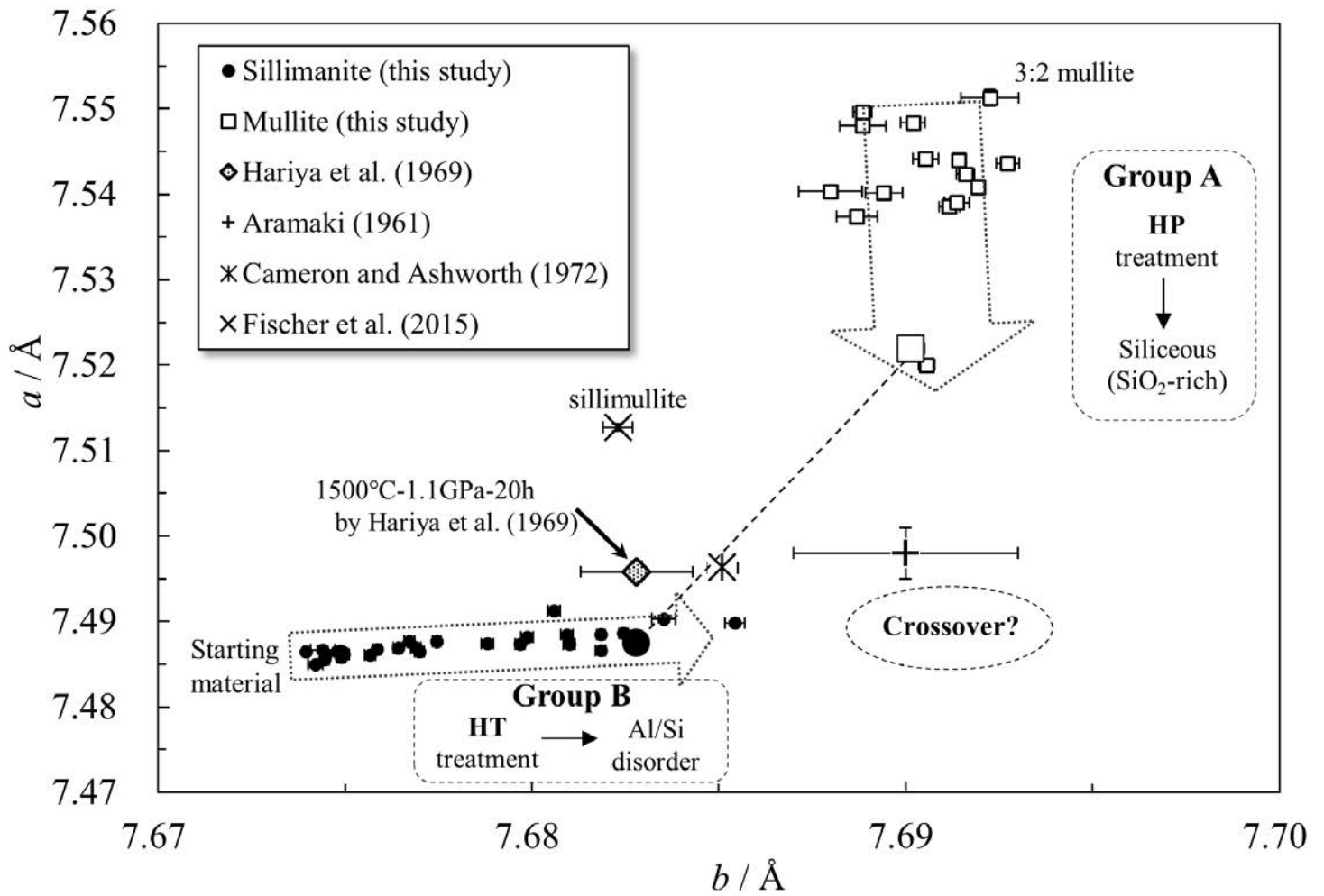


Figure 10



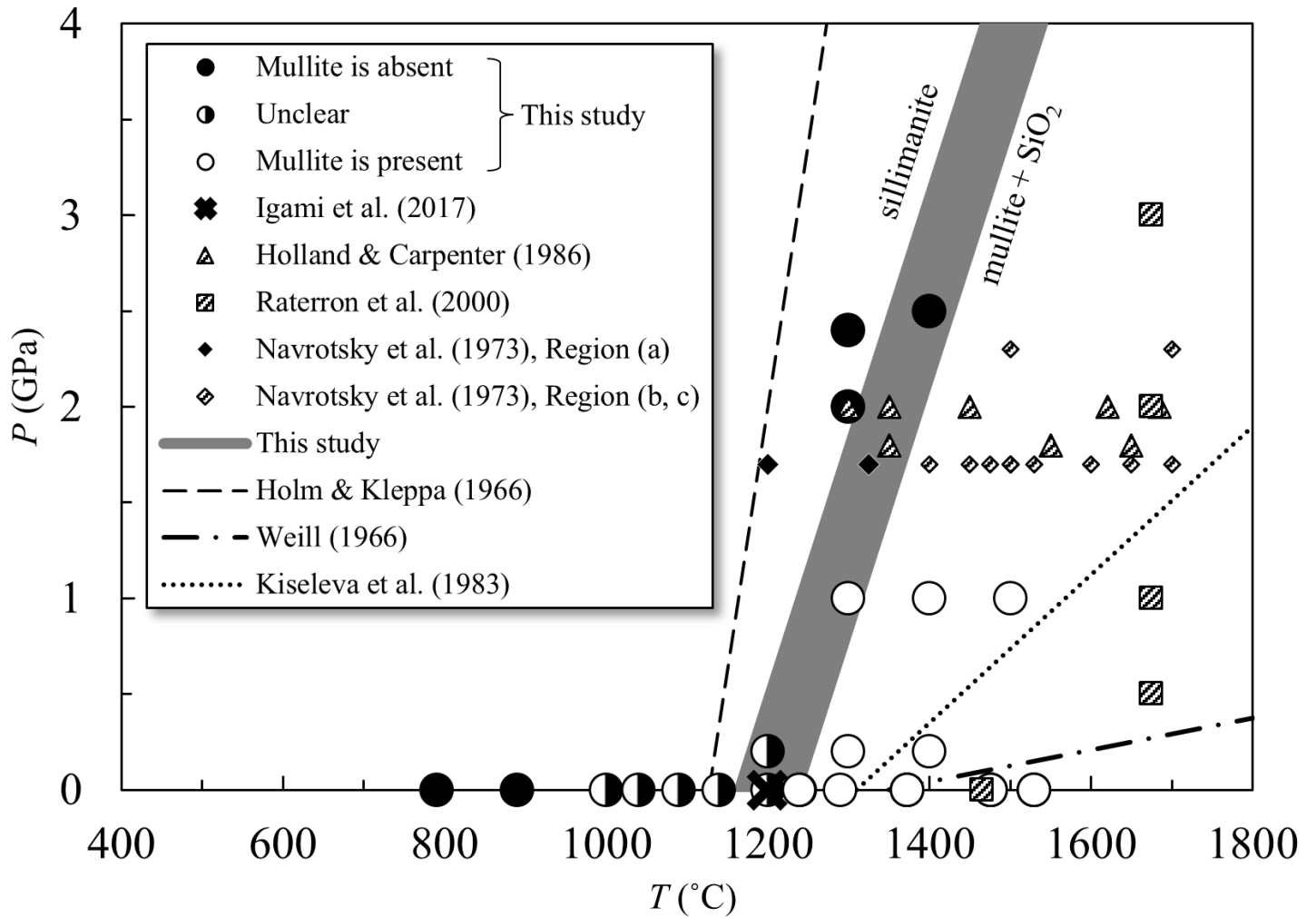


Figure 11

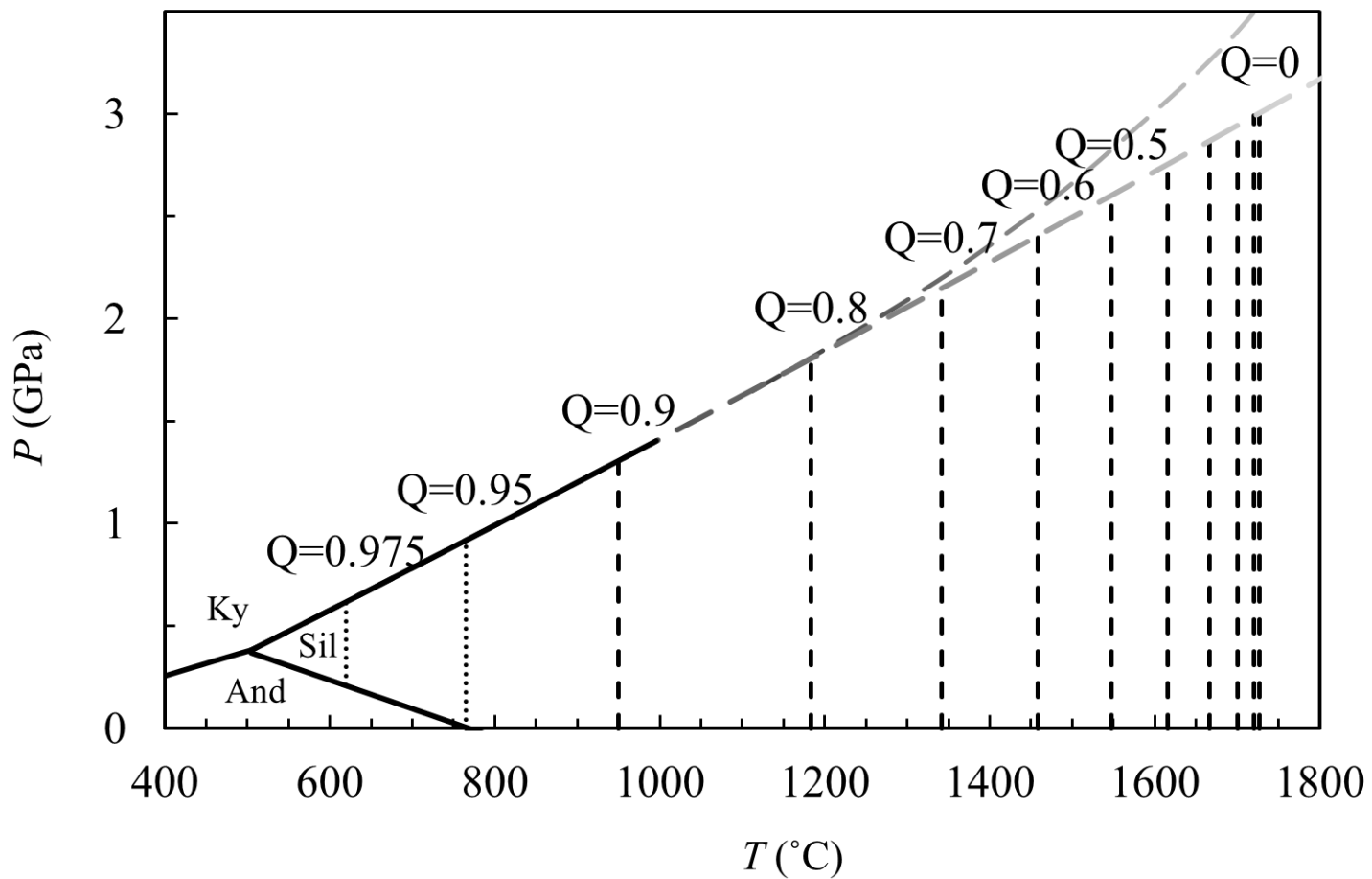


Figure 12